Improving the Spatial Resolution of Land Surface Phenology by Fusing Medium- and Coarse-Resolution Inputs

David Frantz[1*], Marion Stellmes[1], Achim Röder[1], Thomas Udelhoven[1], Sebastian Mader[1] and Joachim Hill[1]

Affiliations:
[1]Environmental Remote Sensing & Geoinformatics, Faculty of Spatial and Environmental Sciences, Trier University, 54296 Trier, Germany.

[*]Corresponding Author:
David Frantz, e-Mail: frantz@uni-trier.de

Reference:
D. Frantz; M. Stellmes; A. Röder; T. Udelhoven; S. Mader; J. Hill, "Improving the Spatial Resolution of Land Surface Phenology by Fusing Medium- and Coarse-Resolution Inputs," in IEEE Transactions on Geoscience and Remote Sensing , vol.PP, no.99, pp.1-12.

DOI: 10.1109/TGRS.2016.2537929
Online available at: http://ieeexplore.ieee.org/xpl/articleDetails.jsp?arnumber=7452606

***Abstract*—Satellite-derived land surface phenology (LSP) serves as a valuable input source for many environmental applications such as land cover classifications and global change studies. Commonly, LSP is derived from coarse-resolution (CR) sensors due to their well-suited temporal resolution. However, LSP is increasingly demanded at medium-resolution (MR), but inferring LSP directly from medium-resolution imagery remains a challenging task (e.g. due to acquisition frequency). As such, we present a methodology that directly predicts medium-resolution LSP on the basis of the respective CR LSP and MR reflectance imagery. The approach considers information from the local pixel neighborhood at both resolutions by utilizing several prediction proxies, including spectral distance and multi-scale heterogeneity metrics. The prediction performs well with simulated data (R^2 = 0.84) and the approach substantially reduces noise. The size of the smallest reliably predicted object coincides with the effective CR pixel size (i.e. field-of-view). Nevertheless, even sub-pixel objects can be reliably predicted provided that pure CR pixels are located within the search radius. The application to real MODIS LSP and Landsat reflectance well preserves the phenological landscape composition, and the spatial refinement is especially striking in heterogeneous agricultural areas, where e.g. the circular shape of center pivot irrigation schemes is successfully restored at medium-resolution.**

***Index Terms*— Data fusion, Landsat, MODIS, phenology.**

I. Introduction

Satellite-derived land surface phenology (LSP) provides important information for land use/cover mapping as well as change detection [1-3], for determining the vegetation response to climate change and variability [4, 5], for usage in large-scale biosphere models [6], and is considered to improve pixel-based composites [7]. The use of LSP has proven to improve the accuracy of derived information compared to single date methodologies, especially in areas where inter-annual LSP variability is high [8].

LSP is commonly derived by using data from coarse-resolution (CR) sensors because of their well-suited temporal resolution of less than 16 days [9]. While LSP derived from these sensors is accepted to be of good quality, its coarse resolution is insufficient to characterize LSP at higher spatial resolution and in heterogeneous areas [10], and as such, CR LSP is less useful for applications that rely on the description of LSP at the landscape level or in highly fragmented landscapes.

On the contrary, inferring LSP directly from medium resolution (MR) imagery like Landsat is a challenging task due to the relatively low acquisition frequency [10], as well due to the substantially reduced data availability in some parts of the world; see e.g. [11]. Whilst the generation of MR LSP is applicable in areas like the United States [10], these methods are inappropriate for areas where the Landsat archive is less densely populated, especially in arid areas where the clear-sky data availability during the wet growing season is virtually zero. As a further constraint, Landsat-based methods are commonly developed in rather stable north American forests and are based on the long-term LSP average from which small annual deviations are inferred [6, 10, 12]. However, inter-annual variations can be significant [13]; for instance burning is widespread in southern Africa [14] and results in an abrupt end of the green season in one year, whereas the season may extend significantly longer in another year if unburnt. A high inter-annual variability in LSP has also been observed over India [15] and Europe [16]. Few approaches exist to infer LSP from actual Landsat time series with methods developed for CR hyper-temporal data, e.g. [17]. Nevertheless, their use is strictly constrained to areas where the Landsat inter- and intra-annual data availability is high and constant; a data density of less than 16 days is needed to describe LSP precisely [9].

Another popular approach is to infer MR LSP (e.g. [18, 19]) in a two-step approach by (i) predicting a time series of synthetic MR surface reflectance images and (ii) applying a CR phenology detection code (e.g. [20]) to this synthetic MR time series. The first step is often approached by employing the spatial and temporal adaptive reflectance fusion model (STARFM: [21]), one of its modifications (e.g. [22, 23]) or regularized spatial unmixing approaches (e.g. [24, 25]). Nevertheless, landscape heterogeneity is known to

decrease STARFM prediction quality substantially, which results in poor image contrast [22], while the enhancement of the modified codes in all environments is as yet inconclusive [26]. Moreover, recent research indicates that a temporal resolution of MR imagery of less than 25 days is eventually needed to ensure high prediction quality [27]. In addition, the technical demand on storage capabilities and processing time is high for large-area projects, since two computationally intensive algorithms are to be applied one after another.

As opposed to existing data fusion techniques, we report on a novel approach that directly predicts LSP at finer resolution on the basis of the respective CR LSP and MR reflectance imagery. The prediction is characterized by great spatial detail and the method avoids the need of predicting a dense time series of MR images in the first step. Southern African (section II) MODIS LSP (III) and Landsat data (III) are used in this study, though the method (presented in section IV) is general enough to be also applied to other sensor pairs and similar continuous fields. An indirect validation is performed with a simulation study by applying the method to an artificial landscape in a controlled, yet realistic setting (VI). Exemplary results of the application to real data are presented in section VII. Relevant issues are directly discussed in the respective later sections (VI, VII) and the key findings are summarized in section VIII.

II. Study Area

The southern African study area includes the countries of Angola, Zambia, Zimbabwe, Botswana and Namibia (~3.7 x 10^6 km²; see Fig. 1) and is centered at the upcoming Kavango-Zambezi Transfrontier Conservation Area (KAZA TFCA). The area is phenologically diverse due to differences in large-scale vegetation cover, primarily as a function of climate gradients. The northwestern part of Angola is located in the tropics and the rainfall decreases southwards due to the temporally shorter influence of the Intertropical Convergence Zone (ITCZ) [28]: the mean annual rainfall is higher than 1500 mm in northern Angola and less than 200 mm (50 mm) in southern Namibia (Namib Desert) [29]. Continentality is also a governing factor, where the Namib Desert is the most arid place due to multiple aridifying effects of climate variables and ocean currents [30]. The vegetation cover ranges from dense Miombo forests in Angola to sparse xerilic savanna ecosystems in the Kalahari, and also includes more extreme surface types like swamps, salt pans and deserts [31]. Being in the southern hemisphere, the phenological cycle of a given year *y* starts with the peak of season (POS), followed by end of season (EOS), minimum of season (MOS) and ends with the start of season (SOS). Fig. 1 displays the POS, EOS and MOS for 2005 – derived from CR data (see III.A). Large-scale differences occur, where especially the Angolan and Western Zambian Miombo forests contrast the southern savanna ecotypes and the more arid Namibian landscapes.

Please place Fig. 1 approximately here.

III. Data

A. Coarse resolution LSP: MODIS

We used the 16-day Vegetation Indices (VI) Dataset at 250 m spatial resolution [32] to capture the CR LSP. The complete time series of the Terra (MOD13Q1) and the Aqua (MYD13Q1) MODIS sensors was incorporated. We used the Enhanced Vegetation Index (EVI) as a proxy for biomass development and the day-of-composite (DOC) information to recreate the actually sensed time series with a nominal temporal resolution of 8 days. The use of the exact acquisition dates can improve LSP accuracy [33]. The DOC was used as the time axis and the VI Usefulness Index [32] was used to weight the data points during the fitting procedure via a damped exponential transfer function. Observations that were flagged as clouds were assigned a weight of zero.

CR LSP was obtained by applying the Spline analysis of Time Series (SpliTS) algorithm [34]. SpliTS is a computer code to fit spline models to remotely-sensed time series and to derive LSP. It is a data-driven method that is able to handle non-equidistant time series and to process the exact DOC. A set of 20 LSP parameters is derived for each pixel, including date-specific parameters, integral information about the

growing seasons, amplitudes, etc. Our prediction approach can handle any of these parameters and simultaneously processes a number of *p* parameters for a given year *y*. CR LSP is reprojected on-the-fly with nearest neighbor resampling to match the extent, projection and resolution of the gridded MR data (see III.B).

B. Medium resolution reflectance: Landsat

We prepared a comprehensive Landsat surface reflectance dataset, which was specifically developed for its use in applications that demand simplified pixel-based access, higher-level radiometric input data and require as many observations as possible [35]. The atmospheric correction module includes radiative transfer code based correction [36] of multiple atmospheric scattering processes [37] with variable illumination/view geometry, a joint database- and image-based estimation of aerosol optical depth (AOD) over dark targets, adjacency effect correction and a spatio-temporally variable water vapor correction using MODIS data. Topographic normalization is achieved by a modified C-correction [38] with 30 m SRTM data. Cloud and cloud shadow detection is performed with a modified version of the Fmask algorithm [35, 39-41]. All available Landsat Level 1T data (Landsat-5, Landsat-7, Landsat-8) were processed, are stored in a gridded data structure in binary image format, and are readily available as input candidates to our prediction algorithm. We define the term 'tile' as an entity of the processing grid and the term 'chip' as the gridded image datasets that are affiliated with a specific tile [35]. 4524 tiles with 1000 x 1000 px (i.e. 194 WRS-2 frames) are needed to cover the study area and 963,563 chips (originating from 20,940 full Landsat images from 2001–2012) were considered to predict MR LSP.

Fig. 2 displays the temporal density of all processed Landsat images per month from 2001–2012. When considering all tiles (Fig. 2*a*), there is usually an observation within four nominal Landsat repeat cycles (i.e. 64 days) throughout the year on average. A large proportion of the data (90% quantile) is characterized by a lower repeat coverage. There is a pronounced seasonality where the repeat coverage in the drier months (May-November) is less than two repeat cycles on average (32 days) and the coverage in the wet season is worse. If only considering tiles that are not part of orbital overlap areas (Fig. 2*b*), the temporal density is significantly worse. The repeat coverage in the drier months reduces to around four repeat cycles and the coverage in the wet season is very poor with an average revisit frequency of 90–100 days or more (December to April). A large proportion of the images (90% quantile) has significantly worse repeat coverage. Due to the relative proximity of the study area to the Equator, orbital overlaps are small, and as such Fig. 2*b* is more important than Fig. 2*a* in assessing if it would be possible to infer LSP reliably from this dataset for the complete area. In addition, the temporal density shown in Fig. 2 was not corrected for cloud coverage, which is high in the wet season and virtually zero in the dry season, and as such would decrease the repeat coverage even more – of a given pixel – in the wet season. The given data density does not allow us to infer LSP directly, especially when considering that the vegetation period coincides with the wet season (roughly November to April).

Please place Fig. 2 approximately here.

IV. Method

The main assumption of our method is that a few MR observations are sufficient to separate image regions with similar phenology qualitatively, but are not suited to quantify LSP directly with high temporal precision – which in turn is possible using CR data. Therefore, we propose that CR LSP can be related to the evolution of reflectance through time at the medium resolution – provided that the MR images are distributed reasonably well over the year. As such, we aim to link the very accurate CR LSP to the corresponding MR spatial features by exploiting their specific spatio-temporal patterns. This is achieved by using the information from the local pixel neighborhood at both resolutions. This approach is somewhat related to the well-known STARFM code [21], though we do not remain in reflectance feature space but directly predict LSP from CR LSP and MR reflectance inputs. Based on a few assumptions on the

reliability of the CR and MR data under different conditions, we define several proxies at both resolutions (subsections *A*-*C*) that define the final neighboring pixel's weight (*D*). In order to increase the computational performance, the MR reflectance data are aggregated prior to the prediction (*E*). The general workflow of the method is outlined in Fig. 3; the corresponding sections are given in the corners of the boxes.

Please place Fig. 3 approximately here.

MR LSP is predicted using a focal filter approach with a circular kernel (kernel diameter $k = 2 \cdot r + 1$ with radius r). All pixels within r are considered to contribute to the prediction. The kernel size is the main tweakable input parameter and controls the level of detail of the prediction as well as processing time.

In principle, the predicted MR LSP for pixel *(x,y)* and LSP parameter p, i.e. $M_{xy,p}$ is obtained by computing the weighted mean of the neighboring CR LSP pixels *(j,i), i.e.* $C_{ji,p}$ with a moving kernel of size k:

$$M_{xy,p} = \sum_{j=1}^{k} \sum_{i=1}^{k} \left(W'_{ji,p} C_{ji,p} \right) / \sum_{j=1}^{k} \sum_{i=1}^{k} W'_{ji,p}, \quad (1)$$

where

(x,y), (j,i), k:	Central pixel, neighbor pixel, kernel size.
p:	Index for LSP parameter.
$M_{xy,p}$:	Predicted medium-resolution LSP of central pixel.
$C_{ji,p}$:	Coarse-resolution LSP of neighbor pixels.
$W'_{ji,p}$	neighbor pixel weight.

Note that the rejection criteria are not accounted for in Eq. (1) for simplicity, e.g. the use of circular kernels.

In order to solve Eq. (1), we need to set up a weight $W'_{ji,p}$ for each neighboring pixel *(j,i)* in order to calculate the MR pixel value at *(x,y)*. As outlined before, we weight the neighboring pixels according to several prediction proxies (*A*-*C*):

A. Spectral distance

As the CR LSP is assumed to be related to the evolution of MR reflectance, a neighboring pixel *(j,i)* should contribute more to the weighted mean if it is spectrally similar to *(x,y)*. The spectral similarity is a proxy for the probability that the adjacent pixel is characterized by similar surface conditions, which increases the probability of phenological similarity. We measure the spectral distance S_{ji} by calculating the Mean Absolute Error (MAE) between the spectra at *(x,y)* and *(j,i)*:

$$S_{ji} = \frac{1}{n_b} \sum_{b=1}^{n_b} \left| \rho_{xy,b} - \rho_{ji,b} \right|, \quad (2)$$

where b is the MR spectral band and n_b is the number of bands (see IV.E for details).

High values of S_{ji} indicate a large spectral distance and should not be used, as *(x,y)* and *(j,i)* do not belong to the same land cover class. Similar to STARFM [21], the prediction is of higher quality if only within-class pixels are used. Nevertheless, there must also be enough pixels to make a good prediction. We use a dynamic cutoff threshold for S_{ji}: S_{max}. We start with an S_{max} of 0.05 MAE, which is a very strict cutoff threshold. If not enough pixels contribute to the prediction, we iteratively increase S_{max} by a factor of 2 until more than n_{min} neighboring pixels are available. Nevertheless, we only allow four iterations to avoid the prediction strength of the weighted mean being weakened too much. We dynamically determine n_{min} based on k, where n_{min} is 0.5% of n_k (the number of pixels in the kernel):

$$n_k = k^2\pi/4 \tag{3}$$

$$n_{min} = 0.5 \cdot n_k/100 \tag{4}$$

Fig. 4 schematically illustrates the prediction process with arbitrary data. The MR reflectance (only one MR band) and the CR LSP are shown in (*a*-*b*). The spectral distance proxy is displayed in Fig. 4*c* and assumes low values for spectrally similar pixels.

Please place Fig. 4 approximately here.

B. Medium resolution heterogeneity

We propose that CR LSP is more representative at the MR scale if the CR sub-pixel heterogeneity is low. Therefore, we compute the spatial heterogeneity for every band in the MR spectral data. The overall heterogeneity score T_{ji} is the heterogeneity metric of the band with the greatest heterogeneity. We use a focal standard deviation filter to infer the heterogeneity with a kernel size of 11 px; the full width at half maximum (FWHM) of the line spread function in the scan direction is approximately 10 MR pixels for the red MODIS band [42], which we rounded to the next odd number. The kernel size is adjustable in order to permit the usage of other combinations of MR/CR data.

The higher T_{ji} is, the more heterogeneous is the CR sub-pixel surface. Fig. 4*d* displays T_{ji} for the arbitrary MR data in (*a*) and T_{ji} is highest where two cover types in the MR data adjoin.

C. Coarse resolution heterogeneity

We propose that CR LSP is also more representative at the MR scale if the CR LSP itself is spatially homogeneous. This is because it is more likely that the CR sub-pixel heterogeneity is low when the pixels are also homogeneous at their inherent resolution. Moreover, if the CR LSP is strongly heterogeneous, there are two adjacent CR pixels that have a substantially different phenology. As the real surface elements (as they would be sensed from an MR instrument) most likely do not match the CR pixel boundaries, the CR pixel boundary area cannot be used to estimate MR LSP reliably. Thus, we also compute the textural heterogeneity of the CR LSP for each parameter *p*. We use the same focal standard deviation filter as in the derivation of the MR texture. This filter accentuates the CR pixel boundaries if they are heterogeneous.

The CR heterogeneity weight $U_{ji,p}$ is the estimated CR texture of *p* at *(j,i)*. The higher $U_{ji,p}$ is, the more heterogeneous is CR LSP. Fig. 4*e* displays U_{ji} for the arbitrary CR data in (*b*) and assumes the highest values in the pixel boundaries where the phenology differs substantially from CR pixel to CR pixel.

D. Neighbor weight

In the next step, the retrieved weights S_{ji}, T_{ji} and $U_{ji,p}$ are rescaled in order to avoid unit scale factors when calculating the total weight and to increase the flexibility of the presented methods when used with different continuous fields. In addition, rescaling increases the contrast between the best and the worst weights through a sigmoidal transfer function for emphasized usage of the best pixels in each kernel. Therefore we apply a range adjustment (the fractional term in Eq. (5)) to the individual weights R_{ji} (S_{ji}, T_{ji} and $U_{ji,p}$) such that all weights range from 0–1, where 0 is the best pixel in the kernel and 1 is the worst. The logistic S-shaped transfer function with range adjustment of the general form

$$R'_{ji} = 1/\left[1 + \exp(25 \cdot \frac{R_{ji} - R_{min}}{R_{max} - R_{min}} - 7.5)\right] \tag{5}$$

is applied to all the weights R_{ji}, where R'_{ji} is the rescaled weight, i.e. S'_{ji}, T'_{ji} and $U'_{ji,p}$. After transforming the weights, $R'_{ji} = 1$ indicates a pixel that should contribute greatly to the prediction; $R'_{ji} = 0$ does not contribute at all.

The final neighbor pixel weight $W'_{ji,p}$ for the phenology descriptor p is then simply the product of the rescaled weights S'_{ji}, T'_{ji} and $U'_{ji,p}$:

$$W'_{ji,p} = S'_{ji} \cdot T'_{ji} \cdot U'_{ji,p}. \quad (6)$$

Fig. 4*f* displays $W'_{ji,p}$, which assumes the highest values in areas where the three proxies S_{ji}, T_{ji} and $U_{ji,p}$ are small. The CR LSP $C_{ji,p}$ in (*b*) is finally averaged with Eq. (1) to predict the LSP of the central pixel, i.e. $M_{xy,p}$. The prediction is indicated by the highlighted MR pixel in (*b*) and is more similar to the pure CR LSP pixels that belong to the same MR land cover class in the bottom-right corner.

E. Aggregation of MR data

We feed the prediction code with MR reflectance from several seasonal windows within the year under consideration *y*. The parameterization of the window lengths and numbers is in control of the user and needs to be adjusted for different study areas. Based on an analysis of the CR LSP and on MR data availability, we defined four windows as they are documented in Table I. They approximate the main climatic seasons and their unequal duration compensates for the uneven MR data availability throughout the year.

Each window is filled with the pixel-mean of all available clear-sky MR images. In a first attempt, only Landsat images that were captured with working Scan Line Corrector (SLC-on) are considered. If SLC-on data are insufficient, SLC-off data are also considered. Occasionally, a window is partly or completely unfilled after this procedure, because there was no valid observation at all. Due to the following statistical procedures, we cannot permit no-data observations, and fill those pixels with the pixel mean of the other windows.

The MR data volume is reduced with a principal component analysis (PCA) of the windowed MR data. All components that explain at least 97.5% of the overall variance are retained. This step is not strictly necessary to produce good results, but it was merely introduced because of performance considerations. Fewer bands decrease the computational cost of obtaining S_{ji} and the PCA retains the information that matters most for the discrimination of spectrally similar pixels. Afterwards, the components are normalized in order to avoid that S_{ji} be merely driven by the 1st component (i.e. the overall contrast) as key information for the discrimination of phenological types is also inherent in other components.

Please place Table I approximately here.

V. Implementation

The code is entirely based on open-source software and is written in C. The application programming interface (API) of the Geospatial Data Abstraction Library (GDAL) is used to reproject the MODIS data to match the Landsat tiles. The PCA was computed using the GNU Scientific Library (GSL) with matrix support provided by the Basic Linear Algebra Subprograms (BLAS) library. Shared memory parallelization was implemented by utilizing the Open Multi-Processing (OpenMP) API. The processing runs on a tile basis. In order to produce a seamless product, we append data of the neighboring 8 tiles to the tile under consideration. The number of appended lines/columns depends on the chosen kernel size *k*.

VI. Algorithm test with simulated data

In order to ensure that the presented approach performs as wanted - within the limits of its assumptions – we performed a simulation study. As such, (i) we generated an artificial simulated landscape that reflects observed landscape characteristics. We (ii) simulated corresponding MR reflectance and (iii) MR LSP based on a statistical analysis of recent Landsat data. CR LSP (iv) was inferred by degrading the MR LSP. We propose our method to be functional if the (v) MR LSP can be reasonably well restored by predicting it from degraded CR LSP and simulated MR reflectance inputs.

(i) Southern African environments are generally composed of large wood-, shrub- and grassland patches with smaller agricultural and urban elements. A random multifractal map (Fig. 5*a*) was generated with QRULE [43], and we manually placed streets and defined six urban seeds. Built-up structures were randomly placed around the streets following a lognormal distribution with a penalty on the distance to the next seed. The structure orientation was inferred from street bearing and the width and height were varied by random numbers for the normal distribution. Constrained by knowledge about the occurrence of agriculture in different land covers as a function of distance to streets and preferably around settlements [44], fields with random sizes and orientations were also randomly placed in the landscape.

(ii) Based on an existing MR classification [44], we extracted class-wise statistics (mean and standard deviation) within the left green, cool dry and hot dry season windows (Table I) from the 2013/14 Landsat-7/8 time series to simulate MR reflectance images (Fig. 5*b*). This was achieved by assigning the class-specific reflectance (+ noise) to the simulated landscape (using normally distributed random numbers while ensuring autocorrelation between the bands). The images were filtered (3 x 3 px lowpass) in order to add spatial autocorrelation and to avoid sharp transitions between land covers to approximate real satellite acquisitions better.

(iii) Class-specific MR LSP statistics were inferred from the 2013/14 Landsat time series (mean and standard deviation). Analogous to (ii), normally distributed random numbers were generated and spatial autocorrelation was added. We exemplarily show results for the EVI amplitude (AMP, Fig. 6*a*) - as this parameter can be inferred from the densified Landsat-7/8 time series with sufficient precision.

(iv) The MR AMP was degraded to 250 m (i.e. CR AMP, Fig. 6*b*) using a MODIS point spread function [42].

(v) Using the degraded CR LSP (iv) and simulated MR reflectance (ii) as input, we predict MR LSP (Fig. 6*c*) and assess if the presented approach is able to restore the simulated MR LSP (iii) reasonably well. The kernel size k was set to 200 px. The difference between simulated and predicted MR LSP is shown in Fig. 6*d,* and the statistical correlation as well as histograms are shown in Fig. 7.

Please place Fig. 5 approximately here.
Please place Fig. 6 approximately here.

The predicted landscape patches are characterized by clearly defined boundaries (Fig. 6*c*) that are even slightly sharper than in the simulated AMP (Fig. 6*a*). AMP values were also predicted with high precision (see Fig. 7, $R^2 = 0.84$). It is very striking that the predicted AMP is less noisy than the inputs (homogeneous appeal in Fig. 6*c*) and the distinct LSP of different land cover classes can be better separated than in the simulated dataset (see the 1D-histograms in Fig. 7). This is caused by the average-based prediction process that strictly uses only the spectrally nearest neighbors. Fig. 6*d* depicts the difference between simulated and predicted AMP; 82.7% of all pixels differ by less than 0.025, which is approximately the error that can be expected from a radiometric pre-processing chain [45]. Nevertheless, there are also many pixels with higher differences, mostly as a result of the difference in noise between simulated and predicted AMP. The differences are highest in the dwarf shrub-/grasslands, which is also the land cover with highest variability in AMP and reflectance inputs; whereas the settlements and dense woodlands have low differences due to their low AMP and reflectance variability. There is also some remaining noise in the predicted AMP (Fig. 6*c*), which occurs because of the noise-induced inseparability of similar land covers (partially overlapping normal distributions in simulated MR reflectance and AMP; see 1D-histogram in Fig. 7). In addition, there are also object size- and distance-related effects that clearly demonstrate the strengths and limitations of the presented approach. It is apparent that the prediction strength of the built-up class (street) rapidly decreases once the distance to the outskirts of the settlement exceeds the radius r (as indicated by the three circles). There were no neighboring pure built-up CR pixels and the street itself was too small (i.e. not even visible in the CR image). Analogously, any object that is smaller than the Field-of-View of the CR instrument (the FWHM of the line spread function in scan direction is approximately 10 MR pixels for the red MODIS band [42]) cannot be precisely predicted if there are no pure CR pixels within r, see e.g. the objects marked

by ‘A’ and ‘B’ in Fig. 6. On the contrary, even very small objects can be predicted with sufficient precision if pure pixels exist nearby (see e.g. ‘C’ in Fig. 6).

Please place Fig. 7 approximately here.

VII. Application to real data

We predicted the POS, EOS, MOS and SOS parameters for the 12 year period from 2001–2012 at Landsat spatial resolution for the entire study area. The kernel size k was set to 200 pixels.

Fig. 8 displays prediction results (*b*) as well as the input CR LSP (*a*) for a phenologically diverse area in Southern Zambia (15.83°S, 27.93°E; R/G/B: POS/EOS/MOS for 2005). The location of the area is indicated by the “+” in Fig. 1. The sugar production in Mazabuka is Zambia’s biggest agricultural site and largest freshwater consumer [46]. Widespread irrigation causes a broad mix of phenology that contrasts against both the naturally occurring woodlands and the riverine vegetation of the Kafue River. The images reveal that the general composition of LSP is adequately preserved in the predicted image, which is also supported by the nearly identical histograms of CR and MR LSP (Fig. 8*c*). The prediction accounts for the mixed pixels in the CR image and has clearly defined object boundaries. This is especially pronounced in the very heterogeneous agricultural areas where e.g. the circular shape of the center pivots or the parcel boundaries were successfully reconstructed (see the enlarged subsets ‘A’ and ‘B’ in the right panel of Fig. 8). Fig. 9 *a-d* and Fig. 10*a-d* depict the MR reflectance input for the four seasonal windows for the subsets ‘A’ and ‘B’, respectively. The data availability was 1-2, 1-2, 4 and 1 SLC-on observations per pixel for the left wet, cool dry, hot dry and right wet season, respectively. The data availability was rather low in most windows, but the approach produces reliable results if at least one high-quality image per phenological key stage is available (as approximated by the seasonal windows). The windowed reflectance images allow for a qualitative separation of image regions with similar phenology. In addition, the MR heterogeneity T_{ji} and the CR heterogeneity $U_{ji,p}$ of the POS, EOS and MOS parameters are also shown in Fig. 9 *e-f* and Fig. 10*e-f*, and indicate pixels that are preferred for predicting the MR LSP (dark colors). The successful restoration of clearly defined MR patches like the agricultural parcels in Fig. 8 supports the validity of the presented procedure and the prediction is characterized by great spatial detail.

Nevertheless, some features that are present in CR LSP are not preserved in the prediction, e.g. the cyan pixels marked by “?”. The temporal resolution of the few input windows might be too low, which would imply that this specific phenological process could not be properly disentangled. The three implemented prediction proxies might also be insufficient in this case, and further inclusion of other proxies might potentially mitigate the mismatch - provided that a further generally valid assumption can be developed. The prediction failed to match the CR LSP with well-defined MR objects that clearly contrast against the surroundings. The mismatch could also be caused by uncertainties in the processing chain of any input data source. The radiometric processing quality of the input Landsat data is generally sound (98.8% of all data was assessed [35] to be within the expected 2.5% algorithm accuracy [45]) – though it cannot be ruled out that single images are not perfectly corrected, which could e.g. be caused by using modeled AOD fallback values in areas where dark targets do not exist [47]. The observed artifacts could also be caused by compositing-related noise in MODIS VI data, which is known to affect the precise determination of LSP [48]. Though the effect of noise is reduced by applying a smoothing spline, remnant artifacts still occur. MODIS VI noise is especially pronounced in arid areas during the rainy season due to the substantially decreased high-quality observation frequency, remaining sensor view angle effects and residual cloud and aerosol contamination [48]. As the simulation (section VI) demonstrated the de-noising capabilities of the presented approach, it is likely that this noise was effectively flattened in the process. Nevertheless, we cannot address the source of this discrepancy with certainty.

Please place Fig. 8 approximately here.

Please place Fig. 9 approximately here.
Please place Fig. 10 approximately here.

VIII. Conclusions

We developed a prediction approach that fuses coarse resolution LSP with medium resolution reflectance imagery. The required medium resolution data density is rather low. Nevertheless, the prediction quality severely decreases if images are not available at several phenological key stages throughout the year. If sufficient temporal sampling is not given any more, the main assumption of the method is violated and areas with similar LSP properties cannot be delineated due to the lack of temporal contrast. This is also the case if the temporal-spectral separability within the pre-defined windows is not sufficient. LSP is directly predicted at the finer scale, and thus the costly need for generating a dense image series at the target resolution is circumvented. The general landscape composition of LSP is well preserved in the prediction, and medium resolution objects are spatially well-defined and have very clear boundaries. LSP values are reliably transferred to the spatial structure at medium resolution. The method implicitly de-noises LSP, yet it preserves sharp edges. The size of the smallest reliably predicted object coincides with the effective size of the coarse resolution pixels (determined by FOV). Nevertheless, even significantly smaller elements can be successfully predicted if there are pure coarse resolution pixels within the search kernel – if not, the prediction strength decreases. The size of the kernel is the most important determinant regarding prediction quality, but also with respect to processing time. The results indicate that the generated medium resolution LSP is well-suited for its further usage. The method was presented to be used with southern African MODIS LSP and Landsat reflectance data, but the method is general enough to be also applied to other study areas, sensor pairs and continuous fields, e.g. SPOT, RapidEye or Sentinel-2 data and above-ground biomass [49].

Acknowledgment

Landsat data courtesy of the U.S. Geological Survey. The MODIS data were retrieved from the online Data Pool, courtesy of the NASA Land Processes Distributed Active Archive Center (LP DAAC), USGS/Earth Resources Observation and Science (EROS) Center, Sioux Falls, South Dakota, https://lpdaac.usgs.gov/data_access/data_pool. KAZA TFCA information and boundary courtesy of Peace Parks Foundation. We thank Anne Schneibel for providing the Landsat classification and information on landscape composition used in the simulation study. The authors also thank the three anonymous reviewers whose helpful comments helped to substantially improve the manuscript.

References

[1] L. Andres, W. A. Salas, and D. Skole, "Fourier analysis of multi-temporal AVHRR data applied to a land cover classification," *International Journal of Remote Sensing,* vol. 15, no. 5, pp. 1115-1121, Mar., 1994; DOI: 10.1080/01431169408954145.

[2] N. A. Brunsell and R. R. Gillies, "Determination of scaling characteristics of AVHRR data with wavelets: Application to SGP97," *International Journal of Remote Sensing,* vol. 24, no. 14, pp. 2945-2957, Jan., 2003; DOI: 10.1080/01431160210155983.

[3] M. Stellmes, A. Röder, T. Udelhoven*, et al.*, "Mapping syndromes of land change in Spain with remote sensing time series, demographic and climatic data," *Land Use Policy,* vol. 30, no. 1, pp. 685-702, Jan., 2013; DOI: 10.1016/j.landusepol.2012.05.007.

[4] M. E. Brown, K. M. de Beurs, and M. Marshall, "Global phenological response to climate change in crop areas using satellite remote sensing of vegetation, humidity and temperature over 26 years," *Remote Sens. Environ.,* vol. 126, no. 0, pp. 174-183, Nov., 2012; DOI: 10.1016/j.rse.2012.08.009.

[5] M. A. White, F. Hoffman, W. W. Hargrove*, et al.*, "A global framework for monitoring phenological responses to climate change," *Geophysical Research Letters,* vol. 32, no. 4, pp. 1-4, Feb., 2005; DOI: 10.1029/2004gl021961.

[6] J. I. Fisher, J. F. Mustard, and M. A. Vadeboncoeur, "Green leaf phenology at Landsat resolution: Scaling from the field to the satellite," *Remote Sens. Environ.,* vol. 100, no. 2, pp. 265-279, Jan., 2006; DOI: 10.1016/j.rse.2005.10.022.

[7] P. Griffiths, S. van der Linden, T. Kuemmerle*, et al.*, "A Pixel-Based Landsat Compositing Algorithm for Large Area Land Cover Mapping," *IEEE J. Sel. Topics Appl. Earth Observ. and Remote Sens.,* vol. 6, no. 5, pp. 2088-2101, Oct., 2013; DOI: 10.1109/jstars.2012.2228167.

[8] D. Simonetti, E. Simonetti, Z. Szantoi*, et al.*, "First Results From the Phenology-Based Synthesis Classifier Using Landsat 8 Imagery," *Geoscience and Remote Sensing Letters, IEEE,* vol. 12, no. 7, pp. 1496-1500, Jul., 2015; DOI: 10.1109/lgrs.2015.2409982.

[9] S. Archibald and R. J. Scholes, "Leaf green-up in a semi-arid African savanna -separating tree and grass responses to environmental cues," *Journal of Vegetation Science,* vol. 18, no. 4, pp. 583-594, Aug., 2007; DOI: 10.1111/j.1654-1103.2007.tb02572.x.

[10] E. K. Melaas, M. A. Friedl, and Z. Zhu, "Detecting interannual variation in deciduous broadleaf forest phenology using Landsat TM/ETM+ data," *Remote Sens. Environ.,* vol. 132, no. 0, pp. 176-185, May, 2013; DOI: 10.1016/j.rse.2013.01.011.

[11] V. Kovalskyy and D. P. Roy, "The global availability of Landsat 5 TM and Landsat 7 ETM+ land surface observations and implications for global 30m Landsat data product generation," *Remote Sens. Environ.,* vol. 130, no. 0, pp. 280-293, Mar., 2013; DOI: 10.1016/j.rse.2012.12.003.

[12] J. I. Fisher and J. F. Mustard, "Cross-scalar satellite phenology from ground, Landsat, and MODIS data," *Remote Sens. Environ.,* vol. 109, no. 3, pp. 261-273, Aug., 2007; DOI: 10.1016/j.rse.2007.01.004.

[13] M. A. White, P. E. Thornton, and S. W. Running, "A continental phenology model for monitoring vegetation responses to interannual climatic variability," *Glob. Biochem. Cycles,* vol. 11, no. 2, pp. 217-234, Jun., 1997; DOI: 10.1029/97gb00330.

[14] W. J. Bond and J. E. Keeley, "Fire as a global 'herbivore': the ecology and evolution of flammable ecosystems," *Trends in Ecology & Evolution,* vol. 20, no. 7, pp. 387-394, Jul., 2005; DOI: 10.1016/j.tree.2005.04.025.

[15] P. M. Atkinson, C. Jeganathan, J. Dash*, et al.*, "Inter-comparison of four models for smoothing satellite sensor time-series data to estimate vegetation phenology," *Remote Sens. Environ.,* vol. 123, no. 0, pp. 400-417, Aug., 2012; DOI: 10.1016/j.rse.2012.04.001.

[16] C. Atzberger, A. Klisch, M. Mattiuzzi*, et al.*, "Phenological Metrics Derived over the European Continent from NDVI3g Data and MODIS Time Series," *Remote Sensing,* vol. 6, no. 1, pp. 257-284, Dec., 2013; DOI: 10.3390/rs6010257.

[17] V. Kovalskyy, D. P. Roy, X. Y. Zhang*, et al.*, "The suitability of multi-temporal web-enabled Landsat data NDVI for phenological monitoring – a comparison with flux tower and MODIS NDVI," *Remote Sensing Letters,* vol. 3, no. 4, pp. 325-334, Jul., 2012; DOI: 10.1080/01431161.2011.593581.

[18] M. Schmidt, T. Udelhoven, T. Gill*, et al.*, "Long term data fusion for a dense time series analysis with MODIS and Landsat imagery in an Australian Savanna," *APPRES,* vol. 6, no. 1, pp. 063512-1-063512-18, May, 2012; DOI: 10.1117/1.jrs.6.063512.

[19] J. J. Walker, K. M. de Beurs, R. H. Wynne*, et al.*, "Evaluation of Landsat and MODIS data fusion products for analysis of dryland forest phenology," *Remote Sens. Environ.,* vol. 117, no. 0, pp. 381-393, Feb., 2012; DOI: 10.1016/j.rse.2011.10.014.

[20] P. Jonsson and L. Eklundh, "Seasonality extraction by function fitting to time-series of satellite sensor data," *IEEE Trans. Geosci. Remote Sens.,* vol. 40, no. 8, pp. 1824-1832, Aug., 2002; DOI: 10.1109/tgrs.2002.802519.

[21] F. Gao, J. Masek, M. Schwaller, *et al.*, "On the blending of the Landsat and MODIS surface reflectance: predicting daily Landsat surface reflectance," *Geoscience and Remote Sensing, IEEE Transactions on,* vol. 44, no. 8, pp. 2207-2218, Aug., 2006; DOI: 10.1109/tgrs.2006.872081.

[22] X. Zhu, J. Chen, F. Gao, *et al.*, "An enhanced spatial and temporal adaptive reflectance fusion model for complex heterogeneous regions," *Remote Sens. Environ.,* vol. 114, no. 11, pp. 2610-2623, Nov., 2010; DOI: 10.1016/j.rse.2010.05.032.

[23] D. Fu, B. Chen, J. Wang, *et al.*, "An Improved Image Fusion Approach Based on Enhanced Spatial and Temporal the Adaptive Reflectance Fusion Model," *Remote Sensing,* vol. 5, no. 12, pp. 6346-6360, Nov., 2013; DOI: 10.3390/rs5126346.

[24] B. Zhukov, D. Oertel, F. Lanzl, *et al.*, "Unmixing-based multisensor multiresolution image fusion," *Geoscience and Remote Sensing, IEEE Transactions on,* vol. 37, no. 3, pp. 1212-1226, 1999; DOI: 10.1109/36.763276.

[25] J. Amoros-Lopez, L. Gomez-Chova, L. Alonso, *et al.*, "Regularized Multiresolution Spatial Unmixing for ENVISAT/MERIS and Landsat/TM Image Fusion," *Geoscience and Remote Sensing Letters, IEEE,* vol. 8, no. 5, pp. 844-848, Apr., 2011; DOI: 10.1109/lgrs.2011.2120591.

[26] I. V. Emelyanova, T. R. McVicar, T. G. Van Niel, *et al.*, "Assessing the accuracy of blending Landsat–MODIS surface reflectances in two landscapes with contrasting spatial and temporal dynamics: A framework for algorithm selection," *Remote Sens. Environ.,* vol. 133, no. 0, pp. 193-209, Jun., 2013; DOI: 10.1016/j.rse.2013.02.007.

[27] M. Förster, T. Schmidt, P. Gartner, *et al.*, "Evaluating the temporal stability of synthetically generated time-series for crop types in Central Germany," in *Analysis of Multitemporal Remote Sensing Images (Multi-Temp), 2015 8th International Workshop on the*, Jul., 2015, pp. 1-4; DOI: 10.1109/Multi-Temp.2015.7245811.

[28] S. E. Nicholson, "Rainfall and Atmospheric Circulation during Drought Periods and Wetter Years in West Africa," *Monthly Weather Review,* vol. 109, no. 10, pp. 2191-2208, Oct., 1981; DOI: 10.1175/1520-0493(1981)109<2191:raacdd>2.0.co;2.

[29] R. J. Hijmans, S. E. Cameron, J. L. Parra, *et al.*, "Very high resolution interpolated climate surfaces for global land areas," *Int. J. Climatol.,* vol. 25, no. 15, pp. 1965-1978, Sept., 2005; DOI: 10.1002/joc.1276.

[30] E. Van Zinderen Bakker, "The origin and palaeoenvironment of the Namib Desert biome," *Journal of Biogeography,* vol. 2, no. 2, pp. 65-73, Jun., 1975; DOI: 10.2307/3038074.

[31] D. M. Olson, E. Dinerstein, E. D. Wikramanayake, *et al.*, "Terrestrial Ecoregions of the World: A New Map of Life on Earth: A new global map of terrestrial ecoregions provides an innovative tool for conserving biodiversity," *BioScience,* vol. 51, no. 11, pp. 933-938, November, 2001; DOI: 10.1641/0006-3568(2001)051[0933:teotwa]2.0.co;2.

[32] A. Huete, C. Justice, and W. Van Leeuwen, "MODIS vegetation index (MOD13)," *Algorithm theoretical basis document,* vol. 3, p. 213, 1999.

[33] A. Bachoo and S. Archibald, "Influence of using date-specific values when extracting phenological metrics from 8-day composite NDVI data," in *Analysis of Multi-temporal Remote Sensing Images, 2007. MultiTemp 2007. International Workshop on the*, Jul., 2007, pp. 1-4; DOI: 10.1109/MULTITEMP.2007.4293044.

[34] S. Mader, "A Framework for the Phenological Analysis of Hypertemporal Remote Sensing Data Based on Polynomial Spline Models," Dr. rer. nat. Ph.D. dissertation, Geographie/Geowissenschaften, Trier University, 2012. [Online]. Available: http://ubt.opus.hbz-nrw.de/volltexte/2012/783/.

[35] D. Frantz, A. Röder, M. Stellmes, *et al.*, "An operational radiometric Landsat pre-processing framework for large area time series applications," *IEEE Transactions on Geoscience and Remote Sensing*, in press; DOI: 10.1109/TGRS.2016.2530856.

[36] D. Tanré, M. Herman, P. Y. Deschamps*, et al.*, "Atmospheric modeling for space measurements of ground reflectances, including bidirectional properties," *Appl. Opt.,* vol. 18, no. 21, pp. 3587-3594, Nov., 1979; DOI: 10.1364/ao.18.003587.

[37] V. V. Sobolev, "Light scattering in planetary atmospheres," *(Translation of Rasseianie sveta v atmosferakh planet, Moscow, Izdatel'stvo Nauka, 1972.) Oxford and New York, Pergamon Press (International Series of Monographs in Natural Philosophy. Volume 76), 1975. 263 p.,* vol. 1, 1975.

[38] S. Kobayashi and K. Sanga-Ngoie, "The integrated radiometric correction of optical remote sensing imageries," *International Journal of Remote Sensing,* vol. 29, no. 20, pp. 5957-5985, Oct., 2008; DOI: 10.1080/01431160701881889.

[39] Z. Zhu and C. E. Woodcock, "Object-based cloud and cloud shadow detection in Landsat imagery," *Remote Sens. Environ.,* vol. 118, no. 0, pp. 83-94, Mar., 2012; DOI: 10.1016/j.rse.2011.10.028.

[40] Z. Zhu, S. Wang, and C. E. Woodcock, "Improvement and expansion of the Fmask algorithm: cloud, cloud shadow, and snow detection for Landsats 4–7, 8, and Sentinel 2 images," *Remote Sens. Environ.,* vol. 159, no. 0, pp. 269-277, Mar., 2015; DOI: 10.1016/j.rse.2014.12.014.

[41] D. Frantz, A. Roder, T. Udelhoven*, et al.*, "Enhancing the Detectability of Clouds and Their Shadows in Multitemporal Dryland Landsat Imagery: Extending Fmask," *IEEE Geosci. Remote Sens. Lett.,* vol. 12, no. 6, pp. 1242-1246, Jun., 2015; DOI: 10.1109/lgrs.2015.2390673.

[42] W. L. Barnes, T. S. Pagano, and V. V. Salomonson, "Prelaunch characteristics of the Moderate Resolution Imaging Spectroradiometer (MODIS) on EOS-AM1," *IEEE Trans. Geosci. Remote Sens.,* vol. 36, no. 4, pp. 1088-1100, Jul., 1998; DOI: 10.1109/36.700993.

[43] R. Gardner and D. Urban, "Neutral models for testing landscape hypotheses," *Landscape Ecol,* vol. 22, no. 1, pp. 15-29, Jan., 2007; DOI: 10.1007/s10980-006-9011-4.

[44] A. Schneibel, M. Stellmes, R. Revermann*, et al.*, " Agricultural expansion during the post-civil war period in southern Angola based on bi-temporal Landsat data," in *Special Volume: Environmental Assessments in the Okavango Region*. vol. Biodiversity & Ecology 5, J. Oldeland*, et al.*, Eds., ed, 2013, ch.; DOI: 10.7809/b-e.00285.

[45] A. Röder, T. Kuemmerle, and J. Hill, "Extension of retrospective datasets using multiple sensors. An approach to radiometric intercalibration of Landsat TM and MSS data," *Remote Sens. Environ.,* vol. 95, no. 2, pp. 195-210, Mar., 2005; DOI: 10.1016/j.rse.2004.12.008.

[46] B. Richardson, "Big Sugar in southern Africa: rural development and the perverted potential of sugar/ethanol exports," *Journal of Peasant Studies,* vol. 37, no. 4, pp. 917-938, Oct., 2010; DOI: 10.1080/03066150.2010.512464.

[47] D. Frantz, A. Röder, M. Stellmes*, et al.*, "On the derivation of a spatially distributed aerosol climatology for its incorporation in a radiometric Landsat pre-processing framework," *Remote Sensing Letters,* vol. 6, no. 8, pp. 647-656, Aug., 2015; DOI: 10.1080/2150704x.2015.1070314.

[48] A. Huete, K. Didan, T. Miura*, et al.*, "Overview of the radiometric and biophysical performance of the MODIS vegetation indices," *Remote Sens. Environ.,* vol. 83, no. 1/2, pp. 195-213, Nov., 2002; DOI: 10.1016/S0034-4257(02)00096-2.

[49] S. S. Saatchi, N. L. Harris, S. Brown*, et al.*, "Benchmark map of forest carbon stocks in tropical regions across three continents," *Proceedings of the National Academy of Sciences,* vol. 108, no. 24, pp. 9899-9904, May, 2011; DOI: 10.1073/pnas.1019576108.

David Frantz received the Diploma degree in applied environmental sciences from Trier University, Trier, Germany, in 2012, with a major in remote sensing. He and is currently working toward the Ph.D. degree at Trier University.

He is currently a researcher with the Department of Environmental Remote Sensing and Geoinformatics, Trier University. His research interests cover the monitoring of dryland ecosystems using multispectral optical remote sensing data. His main research focus is on the radiometric mass pre-processing of remote sensor data, the development and application of data fusion techniques, as well as the development of pixel-based Landsat compositing algorithms for the monitoring of forest dynamics across large areas.

Marion Stellmes received the Diploma degree in applied environmental sciences from Trier University, Trier, Germany, in 2002, with an emphasis on optical remote sensing and geomathematics, and the Ph.D. degree from Trier University, Trier, Germany, in 2011.

She is currently a senior scientist in the Department of Environmental Remote Sensing and Geoinformatics, Trier University. She is interested in interdisciplinary environmental research, particularly in the evaluation of ecosystem goods and services, and has a strong background in remote sensing based monitoring of land degradation and desertification in the Mediterranean and Southern Africa. Furthermore, she is specialized in time series analysis of medium- and coarse-resolution remote sensing time series and has been working for more than ten years in the field of land cover/use change detection.

Achim Röder received the Ph.D degree in natural sciences from Trier University, Trier, Germany, in 2005, for the development of a remote sensing based monitoring framework for Mediterranean rangelands.

He was raised as a geographer, and is currently a senior scientist with the Department of Environmental Remote Sensing and Geoinformatics, Trier University. His general scientific interest is on the integration of optical remote sensing and geospatial data analysis for environmental studies. In particular, he focuses on the assessment of temporal dynamics of land use/cover using change detection and time series analysis techniques and the development of operational spectral mixture analysis concepts. Furthermore, he is interested in analyzing remote sensing based change dynamics to identify driving factors and assess trade-offs in interdisciplinary contexts.

Thomas Udelhoven received the Ph.D. degree from Trier University, Trier, Germany, in 1997.

From 2007 until 2010, he headed the Geomatics platform at the Centre de Recherche Public Gabriel Lippmann in Luxembourg. Since 2010, he is full professor in the remote sensing department with Trier University.

He has been working in the field of remote sensing since 1992, in the framework of many international research projects. His main research topics include time-series analysis, the retrieval of biochemical and structural properties from vegetation and soils using airborne and satellite hyperspectral remote sensing, pattern recognition, and (geo-)statistics. He is author and co-author of many publications in this area.

Sebastian Mader received the Diploma degree in applied physical geography from Trier University, Trier, Germany, in 2006. He received the Ph.D. degree from Trier University, in 2012.

He is currently working as a postdoctoral associate with the Department of Environmental Remote Sensing and Geoinformatics, Trier University. He has a strong background in application programming, databases and statistical data analysis. His main research interest is in the development and implementation of data mining techniques applicable to large remotely sensed data sets.

Joachim Hill received the Ph.D. degree from Trier University, Trier, Germany, in 1991, and the Postdoctoral degree (Habilitation) from Ludwig-Maximilians-University, Munich, Germany, in 1993.

From 1984 to 1994, he was with the Joint Research Centre of the European Commission in Ispra, Italy. Since 1994, he has been a Full Professor of remote sensing with Trier University, Trier, Germany, where he is also the Head of the department of Environmental Remote Sensing and Geoinformatics. He is a member of the scientific advisory group of the Environmental Monitoring and Analysis Program (EnMAP), a German hyperspectral satellite mission to be launched in 2018. His research in remote sensing focuses on data processing strategies for monitoring forest ecosystems and land degradation processes.

Figures

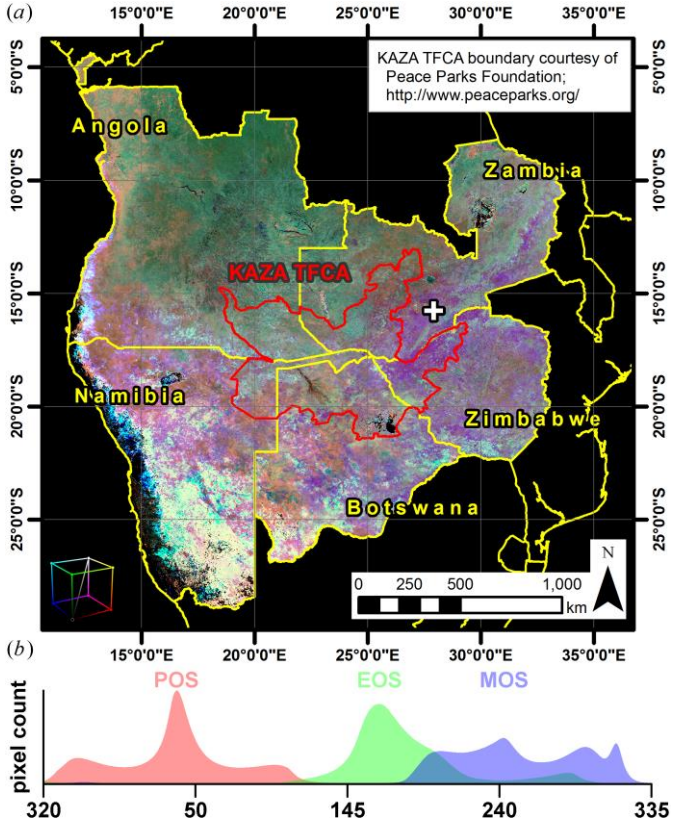

Fig. 1 (*a*): Study area and coarse resolution LSP. KAZA TFCA: Kavango-Zambezi Transfrontier Conservation Area. The RGB-composite depicts the peak of season (POS, red), end of season (EOS, green) and minimum of season (MOS, blue) for 2005. The "+" indicates the subset in Fig. 8. (*b*): Histograms of the depicted data.

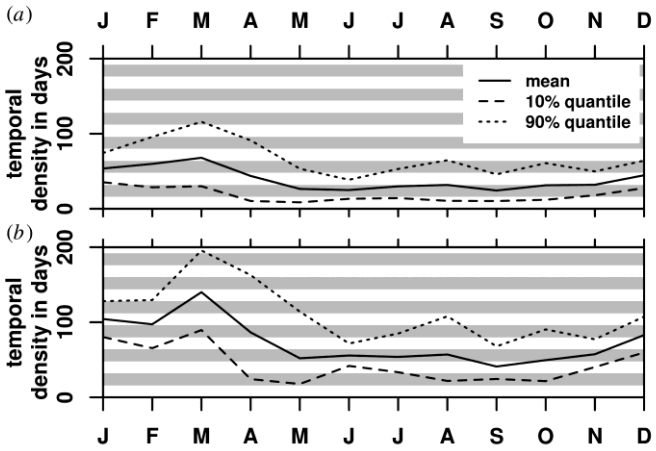

Fig. 2. Temporal density of the available Landsat images per month from 2001–2012. Statistics were calculated per tile and then averaged for the complete study area. (*a*): Temporal density in all tiles; (*b*): Temporal density in tiles that do not have orbital overlaps. The alternating bars in the background indicate intervals of 16 days (nominal nadir repeat coverage of a single Landsat system).

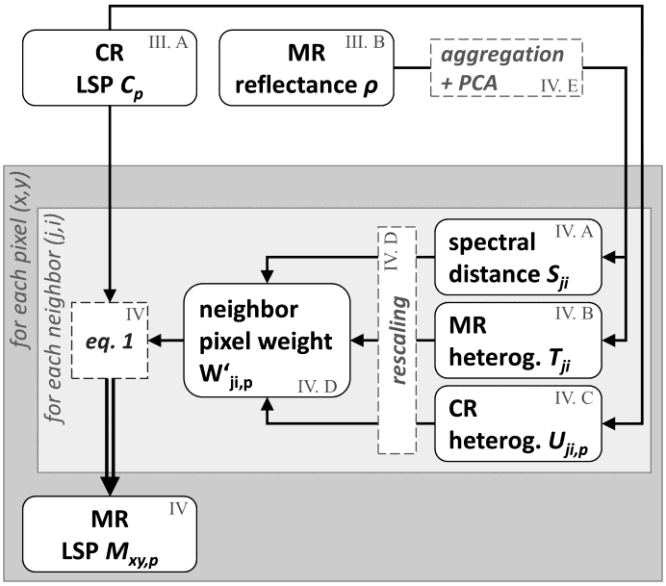

Fig. 3. Workflow of the presented methodology with references to the sections and subsections.

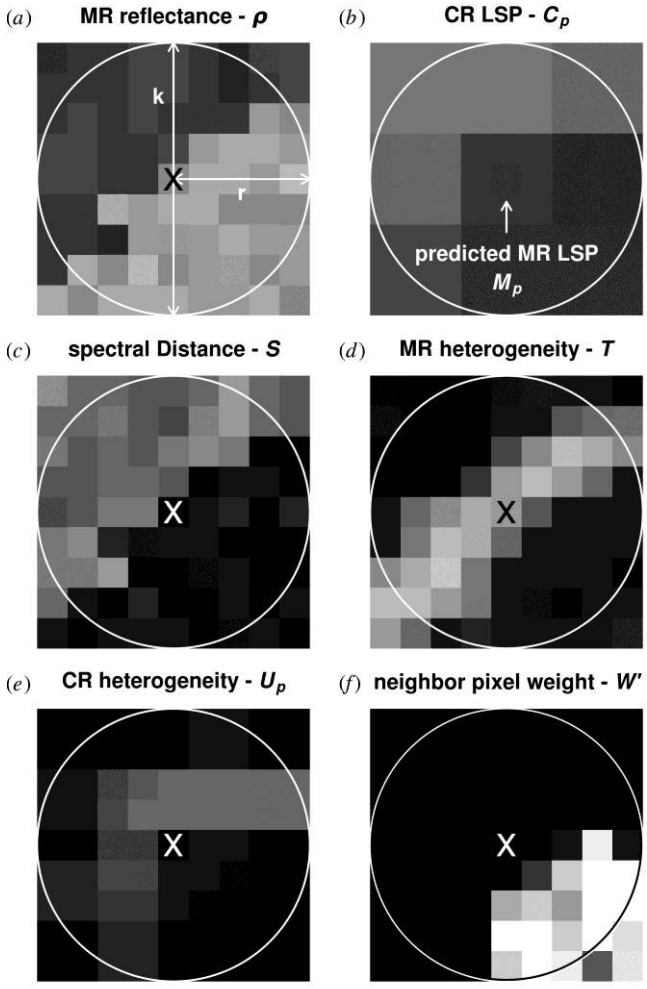

Fig. 4. Schematic illustration of the prediction process. In this example, 1 CR pixel equals 9 MR pixels.

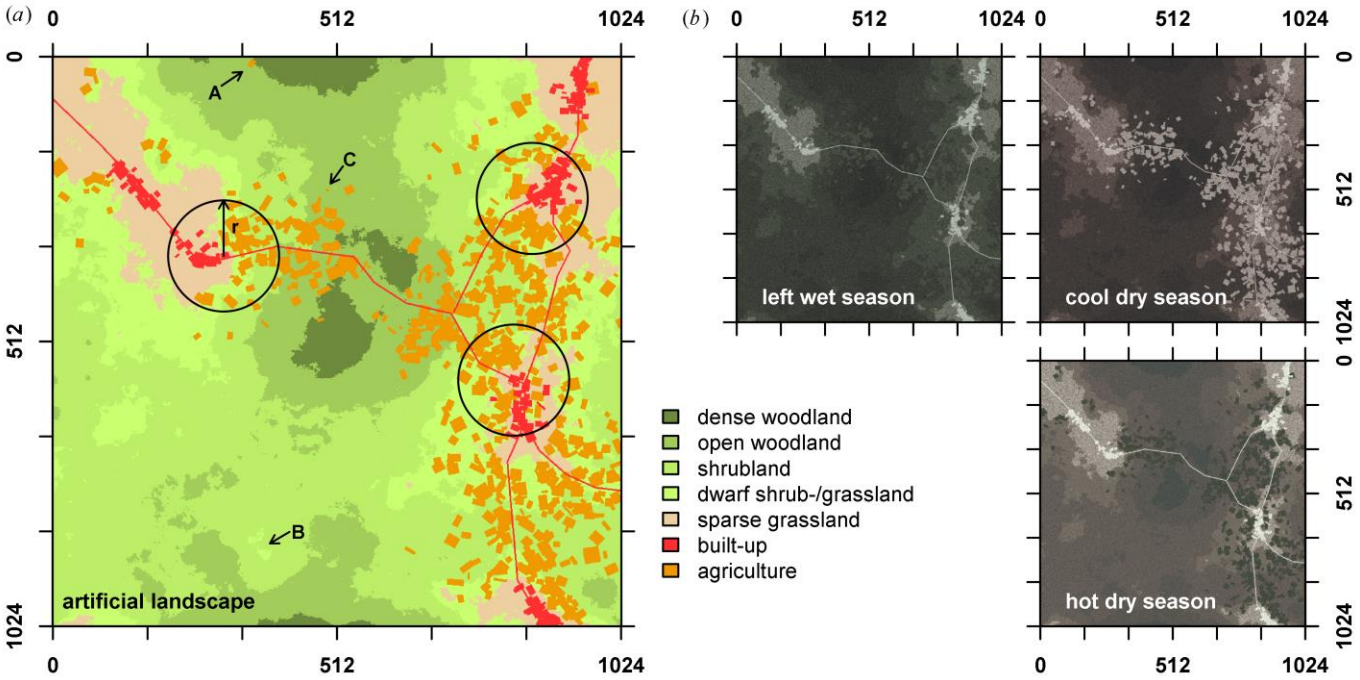

Fig. 5. Simulated random landscape (*a*) and corresponding true color MR reflectance images (*b*) in three seasonal windows (left wet, cool dry and hot dry season). The marked regions in (*a*) are discussed in the text. The same stretch was applied to all images in (*b*). The size of the simulated landscape is 1024 x 1024 px; the prediction radius *r* is 100 px.

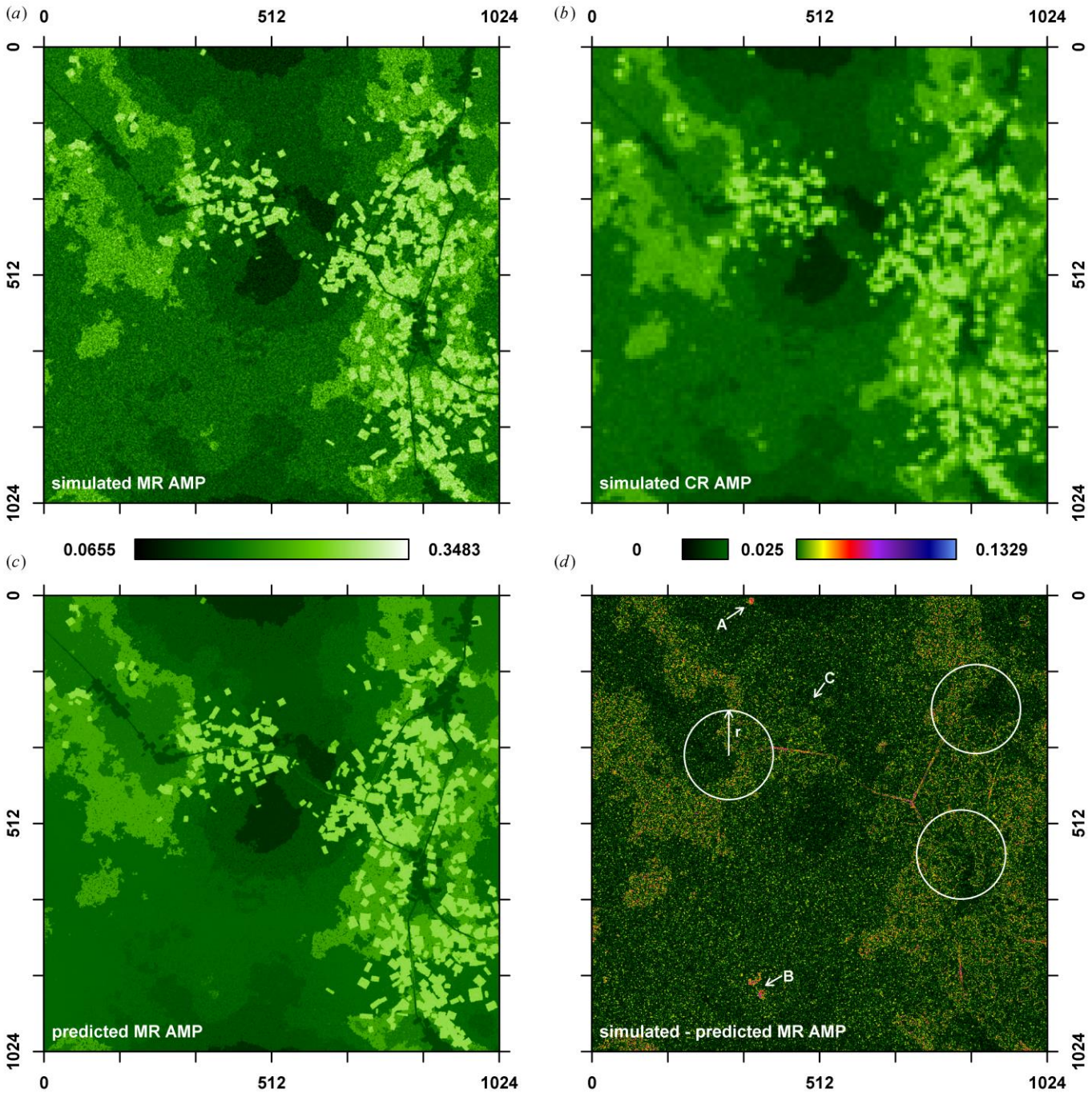

Fig. 6. Algorithm test with simulated data. (*a*) simulated MR amplitude; (*b*) simulated CR amplitude; (*c*) predicted MR amplitude; (*d*) absolute difference between simulated and predicted MR amplitude. The marked regions in (*d*) are discussed in the text and are also shown in Fig. 5*a*. The monochromatic color bar refers to the amplitude values (*a*-*c*) and the right color bar refers to the absolute amplitude difference (*d*). The size of the simulated landscape is 1024 x 1024 px; the prediction radius *r* is 100 px.

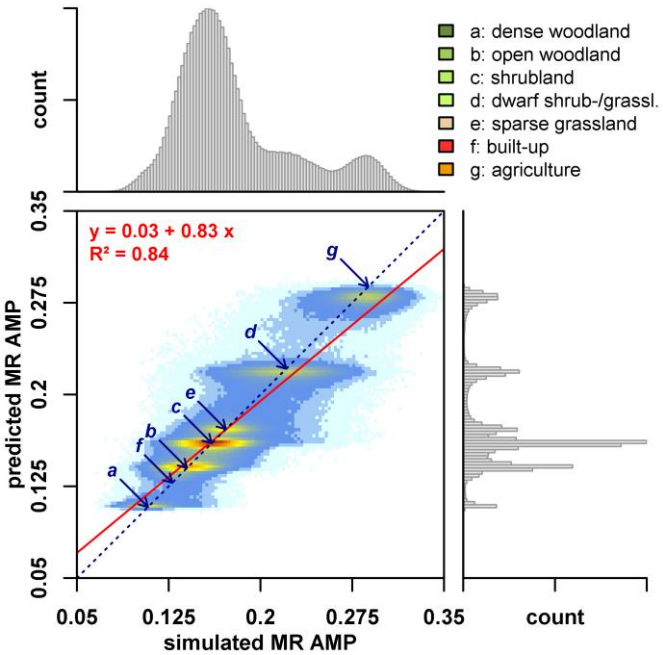

Fig. 7. 2D-histogram of simulated and predicted MR amplitude, bordered by the corresponding 1D-histograms. The letters indicate the simulated land-cover clusters and the legend colors match Fig. 5*a*.

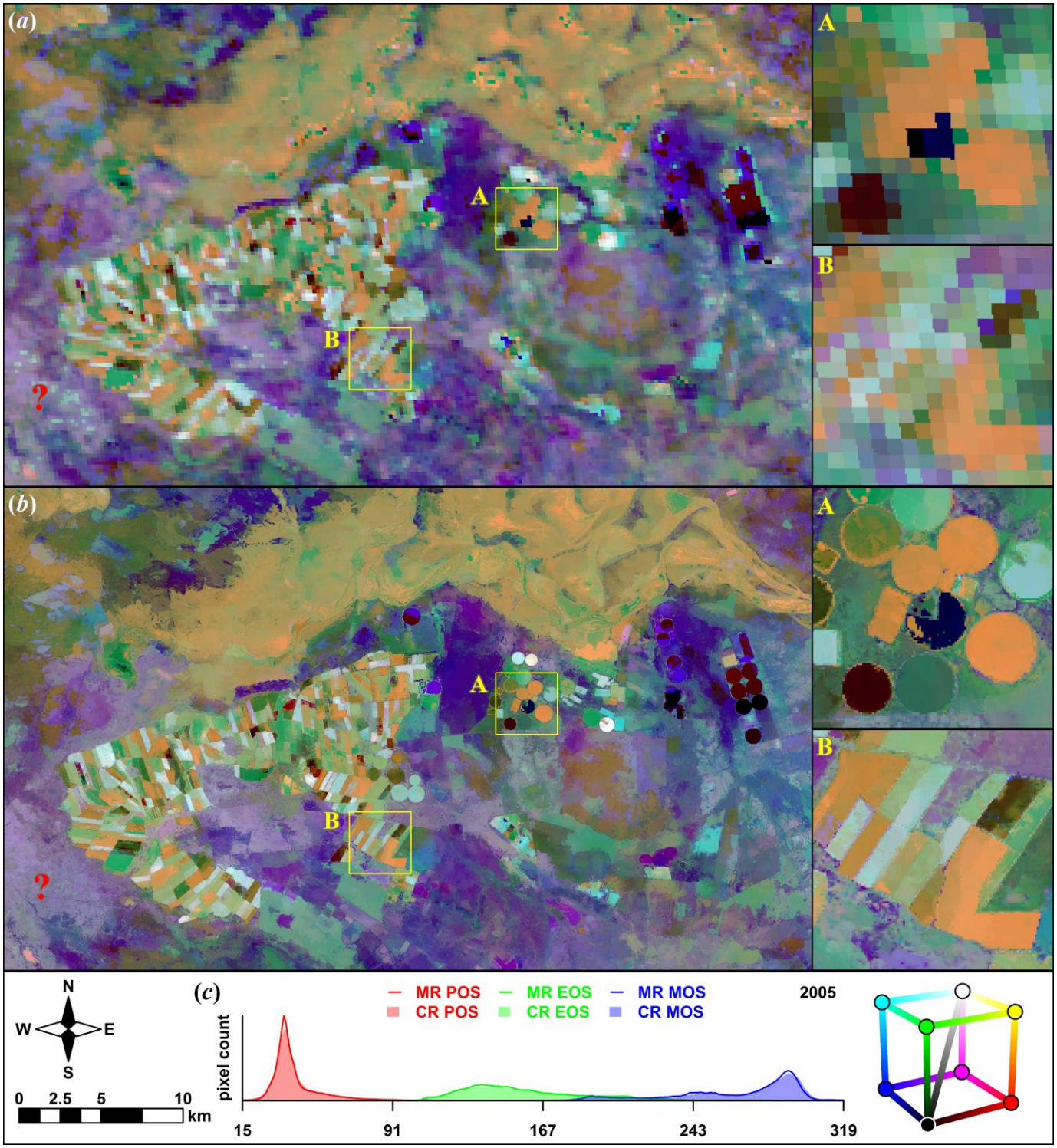

Fig. 8. Comparison of coarse-resolution LSP (*a*) and predicted medium-resolution LSP (*b*). The RGB-composite depicts the peak of season (POS, red), end of season (EOS, green) and minimum of season (MOS, blue) for 2005. Selected areas are enlarged in the right panel (4x zoom). (*c*) Histograms of the depicted data; the lines refer to MR LSP and the polygons to CR LSP.

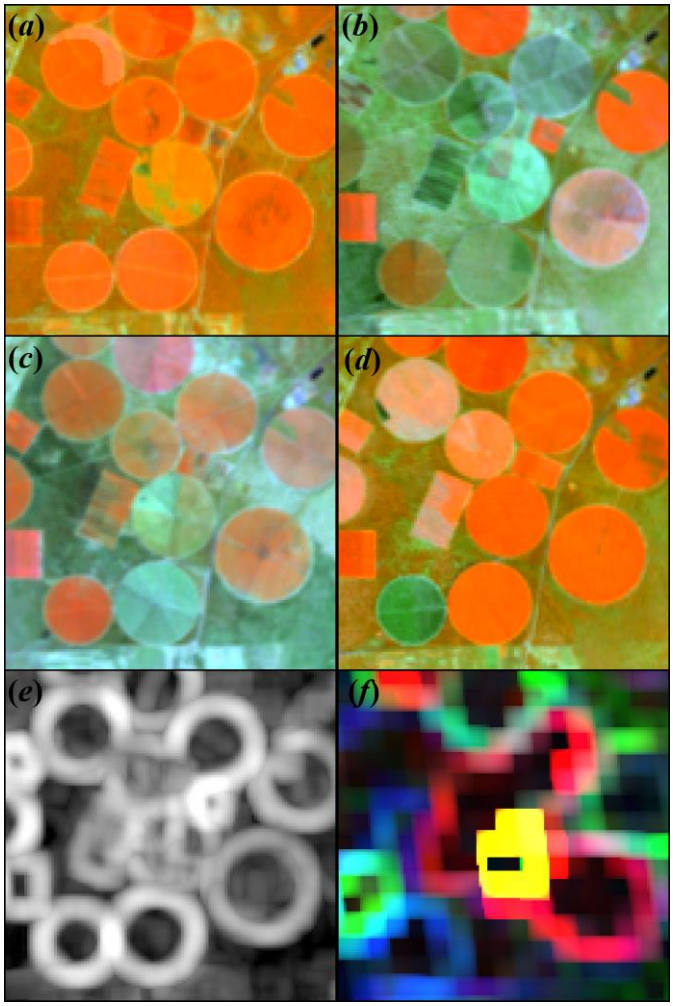

Fig. 9. MR reflectance input data (*a-d*), MR heterogeneity T_{ji} (*e*) and CR heterogeneity $U_{ji,p}$ (*f*) for subset 'A' in Fig. 8. (*a-d*): Average reflectance for the four seasonal windows (Table I) with RGB = near infrared, shortwave infrared, red. The same stretch is applied to all images. (*f*): RGB composite of $U_{ji,p}$ for p = POS, EOS and MOS.

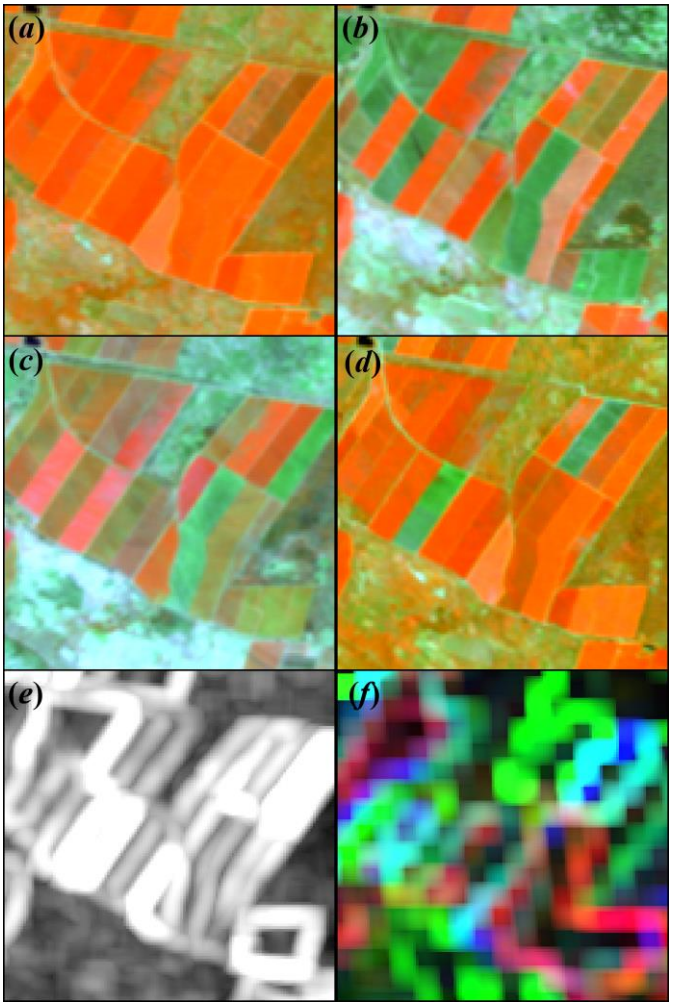

Fig. 10. MR reflectance input data (*a-d*), MR heterogeneity T_{ji} (*e*) and CR heterogeneity $U_{ji,p}$ (*f*) for subset 'B' in Fig. 8. (*a-d*): Average reflectance for the four seasonal windows (Table I) with RGB = near infrared, shortwave infrared, red. The same stretch is applied to all images. (*f*): RGB composite of $U_{ji,p}$ for p = POS, EOS and MOS.

Tables

TABLE I
DEFINITION OF THE SEASONAL WINDOWS

seasonal window	window start	window end
left wet season	312 (-1)	130 (0)
cool dry season	131 (0)	218 (0)
hot dry season	219 (0)	330 (0)
right wet season	331 (0)	130 (+1)

Definition of the seasonal windows used for selecting MR input. Values are day-of-year; the values in the brackets represent the year relative to the year under consideration *y*, which means that the 'left wet season' window starts in the previous year and the 'right wet season' extends to the next year.